

# On the benefits of correcting brightness and contrast in global digital image correlation: Monitoring cracks during curing and drying of a refractory castable

V.F. Sciuti<sup>a</sup>, R.B. Canto<sup>a,b</sup>, J. Neggers<sup>c</sup>, F. Hild<sup>d</sup>

<sup>a</sup>*Federal University of São Carlos (UFSCar)  
Graduate Program in Materials Science and Engineering  
Rodovia Washington Luis, km 235, 13565-905, São Carlos-SP, Brazil*

<sup>b</sup>*Federal University of São Carlos (UFSCar)  
Department of Materials Engineering (DEMa)  
Rodovia Washington Luis, km 235, 13565-905, São Carlos-SP, Brazil*

<sup>c</sup>*Université Paris-Saclay, CentraleSupélec, CNRS  
Laboratoire de Mécanique des Sols, Structures et Matériaux, Gif-sur-Yvette, France*

<sup>d</sup>*Université Paris-Saclay, ENS Paris-Saclay, CNRS  
LMT – Laboratoire de Mécanique et Technologie, Gif-sur-Yvette, France*

---

## Abstract

The gray level conservation is the underlying hypothesis of Digital Image Correlation (DIC). However, it may be challenging to enforce in some experimental configurations. Brightness and contrast corrections (BCCs) may be added to the registration procedure. Different types of BCCs were implemented for global DIC, and their benefits were analyzed for localized and diffuse sources of brightness changes. As a case study to apply BCCs, a refractory castable was placed inside a climatic chamber, and cracks were generated due to localized expansions during its curing and drying. To choose the best BCC for this case, two sets of images were considered. The first one allowed the noise floor levels to be evaluated. The second one dealt with the development of a crack network. The BCCs significantly reduced gray level residuals enabling cracks with small openings to be detected. The coarse discretization was effective in correcting lighting changes and avoided its coupling with the measured kinematic fields and other local phenomena.

**Keywords:** Crack opening displacement, global digital image correlation, brightness and contrast, gray level residuals, uncertainty quantification

---

## 1. Introduction

Digital Image Correlation (DIC) registers images to measure displacement fields on specimen surfaces [1, 2] and in the bulk via digital volume correlation [3, 4]. The displacements may, for instance, be caused by mechanical loads [5] or thermal histories [6]. The images can be 2D [7], generated not only by visible light but also by infrared radiation [8, 9] or electron beams as in Scanning Electron Microscopy (SEM) [10, 11]. They can also be 3D volumes reconstructed from tomographic scans [12, 13].

Two advantages of DIC over conventional extensometry are highlighted. It provides full-field measurements (instead of point-data), and no physical contact is needed between the material and the probe [2, 5]. The first advantage represents an increase of the amount of gathered information. For example, displacement fields of entire surfaces are measured, and not only the crack mouth opening displacement during fracture tests. The correlation between measured fields and close-form solutions can be used to calibrate fracture mechanics parameters [14, 15]. The second advantage enables the technique to be applied to soft materials [16, 17] or at high temperatures [6, 18].

Independently of the image modality, the central hypothesis in DIC techniques is the gray level conservation when the reference and deformed images are matched (*i.e.*, through the determination of the optical flow [19]). Many phenomena can disturb the optical flow, *i.e.*, they can change the gray levels of pixels. Some of them are due to lighting of the experiment [20, 21, 2, 22, 23], drifts of electron beams in SEMs [11, 24], and variations of the refractive index caused by temperature gradients between the imaging device and the sample [18, 25]. The use of lighting with band pass filters [26, 27, 18] mitigated radiation effects due to high temperatures, or working at shorter wavelengths [14] as suggested by Planck's law [28]. Besides the afore-mentioned hardware solutions, software solutions were also implemented very early on [20, 2]. It is worth noting that oftentimes these corrections are uniform over each interrogation window [21, 22, 23] and linear with respect to the reference image. The

Zero-Normalized Cross-Correlation (ZNCC) criterion is one of the most popular  
corrections [29, 21, 2, 22, 23]. For instance, this type of correction was used to  
investigate crack propagation in rocks [30]. Another known correction is a gray  
level average to minimize high temperature effects [31].

Gray level corrections were also introduced in global DIC via brightness and  
contrast field changes [32]. Some specific cases used the gray level corrections,  
for example, DIC analyses of infrared pictures [8, 9], and distortion corrections  
of infrared lenses [33]. Tests performed at temperatures up to 1860°C, for which  
gray level inversions occurred, can also be monitored via global DIC [28]. Such  
procedures were extended to global stereocorrelation to account for illumination  
variations [34], in hybrid multiview correlation to register images of different  
modalities [35]. In digital volume correlation, the determination of metric and  
topological differences on 3D woven composite samples also required gray level  
corrections [36]. Similarly, thanks to such corrections, the gap between modeling  
and analysis could be bridged for 3D woven composites [37].

To study the effect of brightness and contrast corrections in the results of  
global DIC, the monitoring of cracks during curing and drying of an MgO con-  
taining refractory castable was chosen as a case study. The conservation of gray  
levels was disturbed by temperature and air humidity (processing conditions)  
because they alter the refractive index of air [38]. In the field of refractory ma-  
terials, DIC has been applied to their characterization [39, 40, 41, 14], and to  
the detection of initiation and propagation of cracks [42, 43]. For instance, DIC  
was used to analyze drying of mortar [44], and the crack pattern during curing  
and drying of refractory castables [45]. In the present work, small corrections in  
gray levels are proposed since the temperature levels remained less than 60 °C  
but the duration of the test was very long (*i.e.*, 60 h). The corrections are based  
on brightness relaxation, contrast relaxation, or both, to reduce the changes in  
gray level residuals.

As the case study consists in monitoring cracks in a cube made of refrac-  
tory castable put inside a climatic chamber, there are two sources of gray level  
variations, namely, the experimental environment (*i.e.*, temperature and hu-

midity) and the development of crack networks. The corrections were applied to two different sets of images. The first set (set #1) used ten images acquired before crack initiation and investigated the influence of the environment. The second set (set #2) used all the images of the experiment to account for how the corrections affect the quantification of cracks. The outline of the paper is as follows. First, the material, the experiment and the enriched DIC framework are presented. Second, uncertainty quantifications are performed with set #1 for two different discretizations and three different corrections. Third, set #2 is studied by varying the same set of parameters. Their effect on the gray level residuals and maximum principal strain data will be assessed.

## 2. Material and Methods

### 2.1. Refractory castable

The refractory castable studied herein belongs to the group of high alumina refractories [46], and it contains 6 wt.% of caustic magnesia ( $d_{90} < 33 \mu\text{m}$ ). The castable was formulated following the Alfred packing model with  $q = 0.26$ . The raw materials were tabular alumina (Almatis, Germany) and reactive aluminas CL370 and CT3000SG. A polycarboxylate ether-based dispersing agent (Castament<sup>®</sup> FS60, BASF, Germany) was selected. The amount of water was adjusted to provide 80% of the initial flow under vibration [47]. The  $\text{Al}_2\text{O}_3$ -MgO castable formulation is summarized in Table 1.



Table 1: Composition of the studied  $\text{Al}_2\text{O}_3$ -MgO based castable

Raw materials	[wt.%]
Tabular alumina ( $d \leq 6$ mm)	81
Tabular alumina ( $d < 45$ mm)	6
Reactive alumina (CL370)	2
Reactive alumina (CT3000SG)	5
Caustic magnesia ( $\text{SA} = 24.57 \text{ m}^2\text{g}^{-1}$ )	6
Water	5.1
Dispersant	0.2

A cubic specimen of size  $\approx 70 \times 70 \times 70 \text{ mm}^3$  was produced as follows:

- the castable was homogenized for 10 min in a rheometer;
- the mix was cast under vibration into a silicone mold with cavity dimensions of  $70 \times 70 \times 70 \text{ mm}^3$ ;
- the specimen and mold were stored in an in-house developed climatic chamber for 3 h at  $50^\circ\text{C}$  and 50% of air humidity before been unmolded;
- a face was painted using only black paint speckled on the light and matted surfaces to provide contrast for DIC purposes.

More details about the specimen production and the climatic chamber used in the experimental set-up can be found in Ref. [48].

## 2.2. Image acquisition

The hardware parameters of the optical setup are reported in Table 2. An exposure time of 3.2 s was chosen to perform a physical average of the intensity acquired by each pixel [49]. LED lights were put inside the climatic chamber for lighting purposes.

Table 2: DIC hardware parameters

Camera	CANON T5 Rebel
Definition	$3529 \times 5296$ pixels (Bayer pixels)
Color filter	Bayer
Gray Levels amplitude	16 bits
Lens	CANON 100-mm macro
Aperture	$f/22$
Field of view	$65 \times 65 \text{ mm}^2$
Image scale	$50 \text{ }\mu\text{m/pixel}$
Stand-off distance	102 cm
Image acquisition rate	6 fpm (set #1) and 2 fph (set #2)
Exposure time	3.2 s
Patterning technique	sprayed black paint
Pattern feature size <sup>#</sup>	4 pixels (B/W)

<sup>#</sup>evaluated as full width at half maximum of autocorrelation function

The images were acquired as RAW files and then converted to gray scale  
 TIFF images using the Bayer filter [50]. The latter is an assembly of RGB  
 filters arranged as a mosaic with a proportion of 25% red, 50% green, and 25%  
 blue on the camera sensor. The conversion from RAW to TIFF was performed  
 as the average of one red, two green, and one blue levels, which reduces the  
 image definition by a factor  $2 \times 2$ . The time interval between acquisitions was  
 10 s for set #1 and 30 min for set #2 (*i.e.*,  $\approx 200$  images were acquired during  
 the test).

### 2.3. Gray Level Corrections in Global DIC

Global DIC consists in performing registrations over the whole ROI (and  
 not subdividing it into small interrogation windows). The first propositions  
 were based upon spectral decompositions of the displacement field [51, 52].  
 Then, finite element discretizations were considered [53, 54, 55]. The sought

displacement field is written as

110

$$\mathbf{v}(\mathbf{x}) = \sum_i v_i \Psi_i(\mathbf{x}), \quad (1)$$

where  $\Psi_i(\mathbf{x})$  are, in the present case, finite element shape functions, and  $v_i$

111

nodal displacements. The deformed image corrected by such displacement fields

112

becomes

113

$$\tilde{g}_{\{v\}}(\mathbf{x}) = g(\mathbf{x} + v_i \Psi_i(\mathbf{x})), \quad (2)$$

where the column vector  $\{v\}$  gathers all nodal displacements  $v_i$ . In global DIC,

114

the gray level differences are globally minimized over the ROI

115

$$\mathcal{T}_g(\{v\}) = \|\tilde{g}_{\{v\}}(\mathbf{x}) - f(\mathbf{x})\|_{\text{ROI}}^2 \quad (3)$$

such that the sought displacement is the argument that minimizes  $\mathcal{T}_g(\{v\})$

116

$$\{v\}_{\text{DIC}} = \arg \min_{\{v\}} \mathcal{T}(\{v\}). \quad (4)$$

Such writing corresponds to a nonlinear least squares minimization. For in-

117

stance, a Gauss-Newton scheme can be selected. Let us then consider small

118

amplitudes of nodal displacement corrections  $\delta v_i$ , and Taylor expand  $\tilde{g}$  with

119

respect to the current estimate of the nodal displacements  $\{v\}$

120

$$\begin{aligned} \tilde{g}_{\{v\}}(\mathbf{x} + \delta v_i \Psi_i(\mathbf{x})) &= \tilde{g}_{\{v\}}(\mathbf{x}) + \nabla \tilde{g}_{\{v\}}(\mathbf{x}) \cdot \Psi_i(\mathbf{x}) \delta v_i + H.O.T. \\ &\approx \tilde{g}_{\{v\}}(\mathbf{x}) + \nabla \tilde{f}(\mathbf{x}) \cdot \Psi_i(\mathbf{x}) \delta v_i, \end{aligned} \quad (5)$$

where the additional assumption  $\nabla \tilde{g}_{\{v\}}(\mathbf{x}) \approx \nabla \tilde{f}(\mathbf{x})$  was used. With such lin-

121

earization, the approximated least squares functional is quadratic in terms of

122

displacement corrections. Its minimization then leads to a linear system

123

$$[\mathbf{H}]\{v\} = \{\mathbf{j}\}, \quad (6)$$

where  $[\mathbf{H}]$  is the (symmetric semi-definite positive) Hessian, and  $\{\mathbf{j}\}$  the righ-

124

hand side term, whose components read

125

$$\begin{aligned} H_{ij} &= \sum_{\text{ROI}} \left( \nabla \tilde{f}(\mathbf{x}) \cdot \Psi_i(\mathbf{x}) \right) \left( \nabla \tilde{f}(\mathbf{x}) \cdot \Psi_j(\mathbf{x}) \right) \\ j_i &= \sum_{\text{ROI}} \left( \nabla \tilde{f}(\mathbf{x}) \cdot \Psi_i(\mathbf{x}) \right) \rho_{\{v\}}(\mathbf{x}) \end{aligned} \quad (7)$$

with

$$\rho_{\{v\}}(\mathbf{x}) = f(\mathbf{x}) - \tilde{g}_{\{v\}}(\mathbf{x}) \quad (8)$$

the gray level residuals associated with the current estimate of the nodal displacements  $\{v\}$ . Iteratively solving system of equations (6), the nodal displacements and corrected image are updated. The procedure continues until a convergence criterion is reached, namely, the maximum amplitude of the nodal displacement corrections becomes less than a selected threshold (*i.e.*,  $10^{-4}$  px in the present case).

In the above-described procedure, gray level conservation was assumed during optical flow. If such hypothesis is no longer satisfied, the previous residuals  $\rho_{\{v\}}(\mathbf{x})$  can still be lowered in a second step by considering brightness and contrast corrections (with no changes in displacements)

$$\rho_{bcc}(\mathbf{x}) = \rho_{\{v\}}(\mathbf{x}) + q(\mathbf{x}, f), \quad (9)$$

where  $q(\mathbf{x}, f)$  is the gray level correction field that depends on the pixel position  $\mathbf{x}$ , and the gray levels of  $f$ . In the present work, the first two terms are selected

$$q(\mathbf{x}, f) \approx b(\mathbf{x}) + c(\mathbf{x})f(\mathbf{x}) \quad (10)$$

and correspond to the brightness correction field  $b$ , and contrast correction field  $c$ . Such hypothesis leads to an affine model at the pixel level, which is commonly performed at the subset level in local DIC [20, 21, 2, 22, 23], yet generally not written in this form. In the following, non uniform corrections are considered. Various spatial approximations were proposed [32, 33, 9, 36]. Finite element discretizations were selected for the sake of simplicity and adaptability. As for the displacement field, the two correction fields are written as

$$b(\mathbf{x}) = \sum_k b_k \theta_k(\mathbf{x}) \quad \text{and} \quad c(\mathbf{x}) = \sum_k c_k \theta_k(\mathbf{x}), \quad (11)$$

where  $\theta_k(\mathbf{x})$  are (scalar) finite element shape functions,  $b_k$  nodal brightness and  $c_k$  nodal contrast corrections. The latter ones are obtained by minimizing the L2-norm of  $\rho_{bcc}$  with respect to the column vector  $\{\varsigma\}$  gathering all corrections  $b_k$

and  $c_k$ . In the present case, a standard least squares minimization is performed (i.e., no iterations are needed). From these estimates, a corrected reference image  $\hat{f}$  is computed

$$\hat{f}(\mathbf{x}) = b(\mathbf{x}) + (1 + c(\mathbf{x}))f(\mathbf{x}) \quad (12)$$

and instead of using  $f$  in the first DIC step, the corrected reference image  $\hat{f}$  is considered. Therefore, a staggered algorithm is used to minimize  $\rho_{bcc}(\mathbf{x})$ , namely, first minimizing  $\rho_{\{v\}}(\mathbf{x})$  for given gray level corrections, and then  $\rho_{bcc}(\mathbf{x})$  at fixed nodal displacements  $\rho_{\{v\}}(\mathbf{x})$ . These two steps are repeated until final convergence [36]. In the present case, final convergence is still checked on the maximum amplitude of the nodal displacement corrections (to become less than  $10^{-4}$  px). All the results reported herein satisfied the convergence criterion in less than 200 iterations. This rather large number is due to the complexity of the studied phenomenon (i.e., crack network) in comparison with the very low displacement threshold, and the coupling between BCC and DIC steps.

It is worth noting that the shape functions of BCCs (Equation (11)) do not need to be identical to those used in the kinematic basis (Equation (1)). Consequently, the scale at which the displacement field is discretized can be different from that associated with brightness and contrast corrections. This remark shows that the present framework is adaptable to various situations. Two very different discretizations are studied hereafter.

#### 2.4. Correction types

In the following analyses, three different types of gray level corrections were used, namely only brightness correction (B), only contrast correction (C), brightness and contrast (BC) corrections. Two discretizations were used, namely one 8-noded quadrilateral element (Q8) with the same size of the ROI. This Q8 element was used to perform gray level corrections taking into account the variations of brightness and contrast over the entire surface (i.e., with eight degrees of freedom (DOFs) per corrected component). A fine mesh (FM) composed of 3-noded triangular elements (T3) was used with an average size of 5 px. This

mesh is made of 40,000 nodes. This second mesh was also utilized for the discretization of the displacement fields (*i.e.*, DIC + BCCs) and for the analyses with no correction (*i.e.*, no BCC).

The fine mesh can be seen in a zoomed zone shown in Figure 1. Such mesh covers the whole ROI but the elements are too small to be displayed in the reference image with no zoom. The results were designated by a tag as no BCC (*i.e.*, no applied correction), and the mesh used in the correction followed by the type of correction. For example, Q8 B means only brightness correction using the 8-noded quadrilateral element.

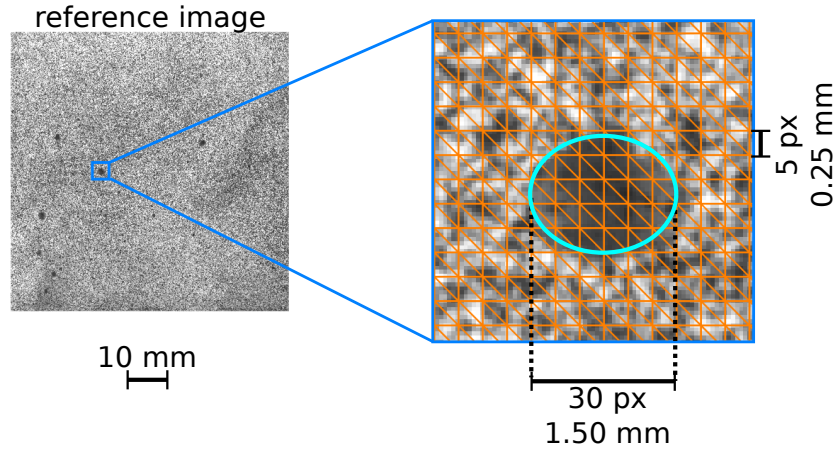


Figure 1: Reference image used in the DIC analyses with an indication of the ROI and a zoomed zone containing one open pore

The images were processed using the Correli 3.0 framework [56] in which BCCs were implemented (Table 3).

Table 3: DIC analysis parameters

DIC software	Correli 3.0 [56]
Image filtering	none
Element length	5 pixels
Shape functions	linear (T3)
Mesh	regular (see Figure 1)
Matching criterion	see text
Interpolant	cubic
Displacement noise-floor	see Table 4
Strain calculation	derivative of shape functions
Strain noise-floor	see Table 4

### 3. Results

#### 3.1. Uncertainty quantification

The effect of the experimental set-up in terms of gray level fluctuations and corresponding measurement uncertainties was analyzed using the image set #1. Each image was used as one reference, while the other nine as “deformed” pictures. This permutation resulted in 81 pairs analyzed by applying the three corrections, each one using the two discretizations as described in Section 2.4.

In the following, the RMS nodal residuals are reported. They correspond to the integration of the gray level residuals  $\rho_{\{v\}}$  weighted by the shape functions associated with each node of the finite element mesh. They were subsequently normalized by the dynamic range of the reference image for DIC with no BCC and compared to their counter-parts provided by DIC + BCC (*i.e.*,  $\rho_{bcc}$ ) using Q8 (Figure 2(a)), or FM discretization (Figure 2(b)). If there is no effect using the BCC procedure, then the data should lie on the 45° line. Further, the values of  $\rho_{bcc}$  resulting from the two discretizations used in the BCCs are compared in Figure 2(c).

The results for  $\rho_{bcc}$  with the three corrections and the two discretizations mostly lie below the 45° line, thereby proving that the BCCs reduced the overall

gray level residuals. This result shows that the BCC procedure is beneficial to the reported DIC analyses. For the Q8 element, C and BC corrections achieved lower levels in comparison to B corrections (Figure 2(a)). For the FM mesh, the analyses using B or BC corrections led to lower residuals than that using C correction only (Figure 2(b)). This difference in general trend is confirmed in Figure 2(c). Because more DOFs are available for BC corrections with respect to B or C, the residuals could be reduced more significantly. However, the results for BC corrections are very close irrespective of the number of DOFs.

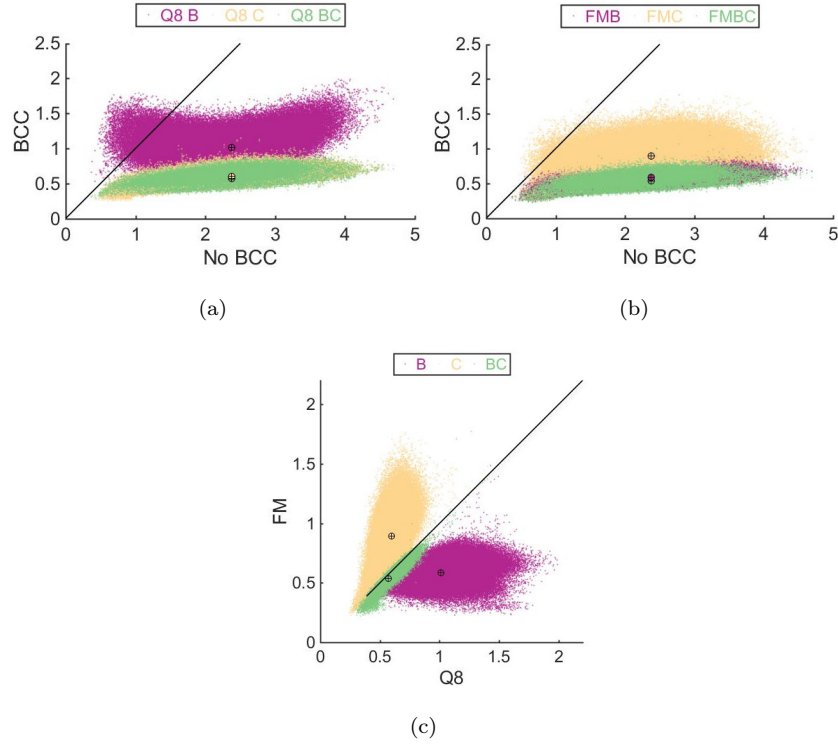


Figure 2: Normalized nodal residuals associated with  $\rho_{bcc}$  (expressed in % of the dynamic range) for each type of correction: brightness (B), contrast (C), brightness and contrast (BC) compared with DIC residuals with no BCC (computed from  $\rho_{\{v\}}$ ). Two different discretizations were considered in the corrections. (a) Effect of BCCs using the Q8 element, and (b) the fine mesh (FM). (c) Comparison between the results obtained with both discretizations. The circled crosses depict the mean level of each case



In Figure 2(c), the residuals obtained with both discretizations used for BCCs are compared. The results are close to the 45° line. The FM discretization performs better when applied with correction B than with C in which the results lie above the 45° line. It can be a consequence of the coupling between C corrections and the underlying kinematics because the same mesh is used for both of them. Besides, BC corrections performed equally well with the two discretizations. The fact that the residuals remain close allows the global BCC with a single Q8 element to be validated in addition to the FM discretization.

The same comparison procedure and permutation of images of set #1 was used to study the standard displacement uncertainties, which are reported in Figure 3.

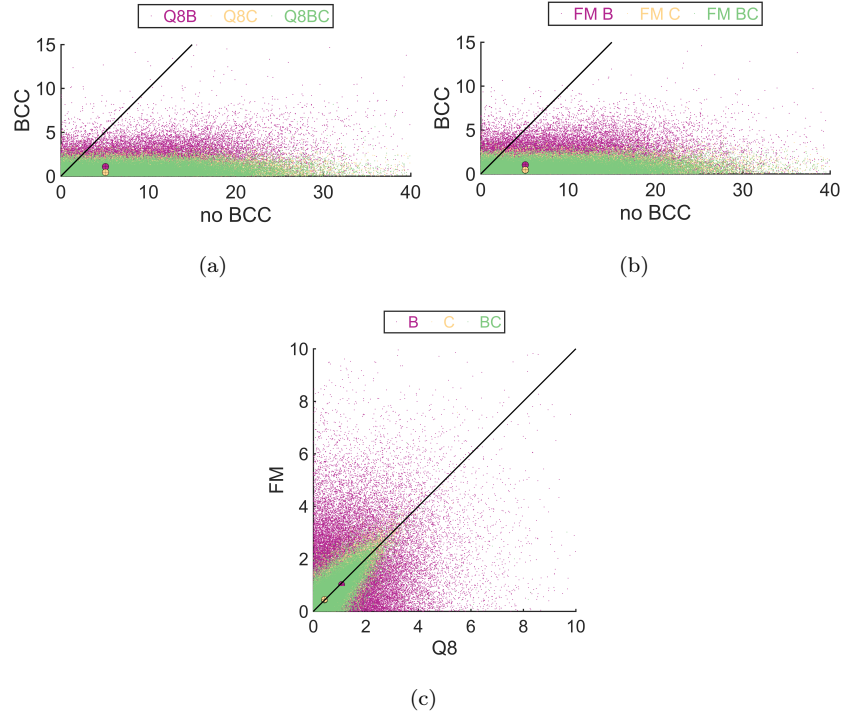


Figure 3: Standard nodal displacement uncertainty (expressed in cpx) for each correction: brightness (B), contrast (C), as well as brightness and contrast (BC). The corrections were applied using different discretizations: (a) Q8 element and (b) fine mesh (FM). (c) Comparison between the two discretizations. The circled crosses depict the mean level of each case

Only the horizontal component of the nodal displacements is reported since the  
same levels were found for the vertical component. The small level is a result  
of acquiring the images at the very beginning of the experiment, before crack  
network initiation (*i.e.*, it allows for an estimation of the noise-floor levels). Fur-  
ther, the short time intervals (*i.e.*, 10 s) between acquisitions reduce the amount  
of drift that may occur. Thus, in addition to acquisition noise, brightness dif-  
ferences (due to illumination variations) are the main source of displacement  
fluctuations for image set #1. The standard deviation of each nodal displace-  
ment was computed thanks to the 81 analyses, and then it was averaged over  
all considered nodes for various corrections.

Figures 3(a,b) show that there is a significant reduction (*i.e.*, one order of  
magnitude) in standard displacement uncertainty for any of the applied correc-  
tions and the two discretizations in comparison to DIC with no BCC. In the  
present case, the C and BC corrections are more effective than B (Figure 3(c)).  
Such observations apply to both discretizations. The fact that the gray level  
residuals could be reduced in addition to achieving lower displacement uncer-  
tainties validates the BCC procedures in the present experimental configuration.

The case study discussed herein consists of monitoring and quantifying cracks  
induced by curing and drying. Therefore, the maximum principal strain field  
is one of the essential quantities to analyze since it can be related to the crack  
opening displacement [45, 48]. With the selected elements (*i.e.*, T3), the strains  
are uniform over each element. These values were considered with no filter-  
ing, and the in-plane principal strains were computed, of which the maximum  
level was selected since cracks are detected with this quantity [13]. Figure 4  
shows that the general trends are very close to those observed with displace-  
ment data (Figure 3) since strain uncertainties are proportional to displacement  
uncertainties [57].

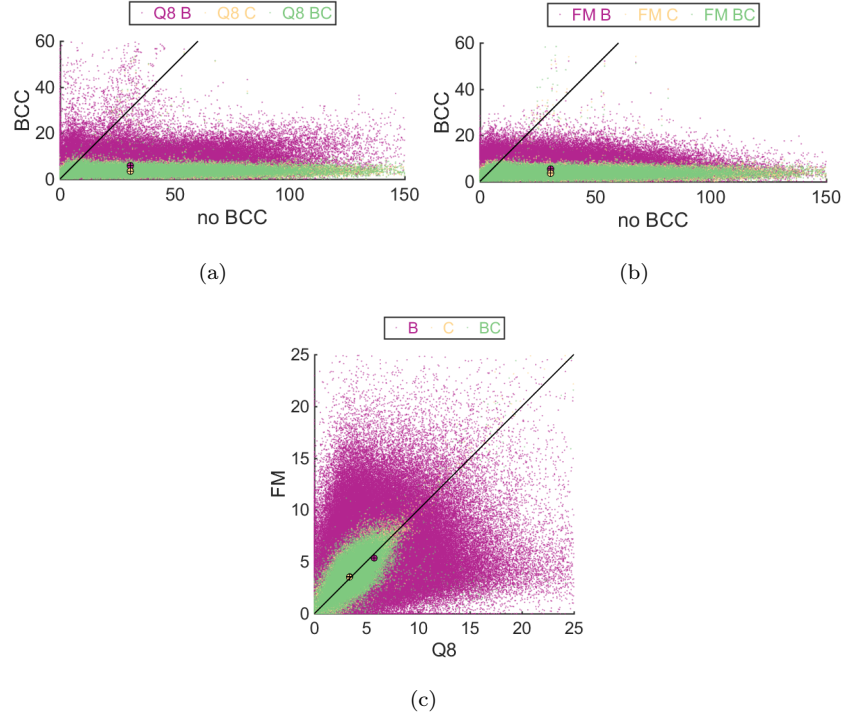


Figure 4: Standard deviation of the maximum principal strain (expressed in %) for each correction type: brightness (B), contrast (C), brightness and contrast (BC). The corrections were applied using different discretizations: (a) Q8 element and (b) fine mesh (FM). (c) Comparison between the two discretizations. The circled crosses depict the mean level of each case

The previous results are summarized in Table 4. For both discretizations  
studied herein, the BC correction leads to the lowest gray level residuals. For the  
displacement and strain uncertainties, the coarse discretization provides slightly  
lower levels. This observation means that, in the present case, the increase in  
DOF (FM) is irrelevant for the gray level variations, which uniformly affect the  
surface of interest, and the Q8 discretization is sufficient. The latter has a scale  
separation with the kinematic basis that will avoid couplings between the two  
steps of the registration procedure.

Table 4: Normalized root mean square of gray level residuals ( $\rho$ ), standard displacement ( $u_x$ ) uncertainty, and corresponding levels for the maximum principal strain ( $\varepsilon_1$ )

Analyses	RMS( $\rho$ ) [%]	std( $u_x$ ) [cpx]	std( $\varepsilon_1$ ) [% <sub>00</sub> ]
DIC (w/ no BCC)	2.4	5.1	30.6
DIC + Q8 B	1.0	1.1	5.8
DIC + Q8 C	0.6	0.4	3.4
DIC + Q8 BC	0.6	0.4	3.4
DIC + FM B	0.6	1.0	5.4
DIC + FM C	0.9	0.5	3.5
DIC + FM BC	0.5	0.4	3.6

### 3.2. Applying BCCs to curing and drying experiment

The BCC procedure was applied to image set #2 during curing and drying of the refractory cube. The discretizations and DIC parameters were the same as those used in set #1 (Table 3 and Figure 1). The gray level residual  $\rho_{\{v\}}$  and maximum principal strain  $\varepsilon_1$  fields obtained with DIC with no BCC are shown in Figure 5 for the last acquired image of the experiment (*i.e.*, when the crack network is the most developed). Both fields show the presence of cracks. They appear as high absolute gray levels in the residual field because they do not satisfy displacement continuity and new gray levels are created by their opening. The elements located on the cracks lead to a high value of maximum principal strain. Both fields are grainy, which indicates the presence of fluctuations affecting them.

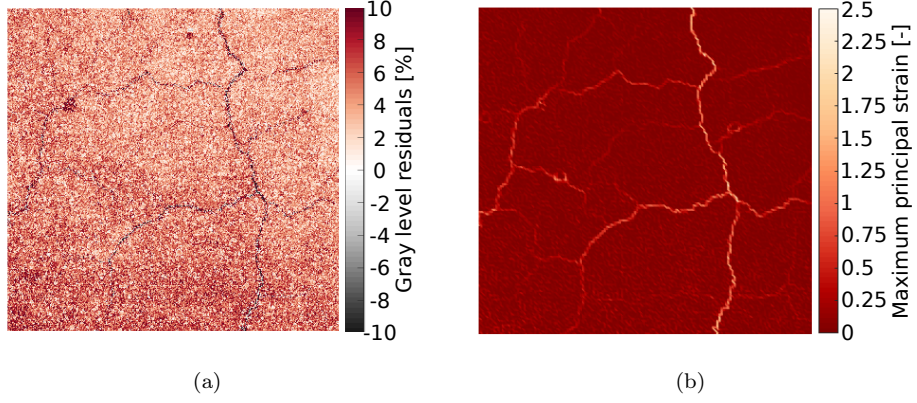


Figure 5: (a) Gray level residuals (in % of dynamic range) and (b) maximum principal strain (dimensionless) field for the last image acquired during curing and drying of the refractory cube

Figure 6 shows the gray level residual fields  $\rho_{bcc}$  when BCCs were applied. 272  
The use of B and BC corrections for Q8 and FM discretizations significantly 273  
reduced the levels of the residual field, when the BCCs results are compared 274  
to those with no BCC (see Figure 5). The regions without cracks presented 275  
very low levels  $\approx 0.05\%$  (Figure 6(a,b,e,f)). When only C corrections were 276  
applied, both Q8 and FM results induced gray level residual fields similar to 277  
that provided by DIC with no BCC. These fields are very grainy, which makes 278  
the larger cracks barely distinguishable (Figure 6(c,d)) for both discretizations. 279

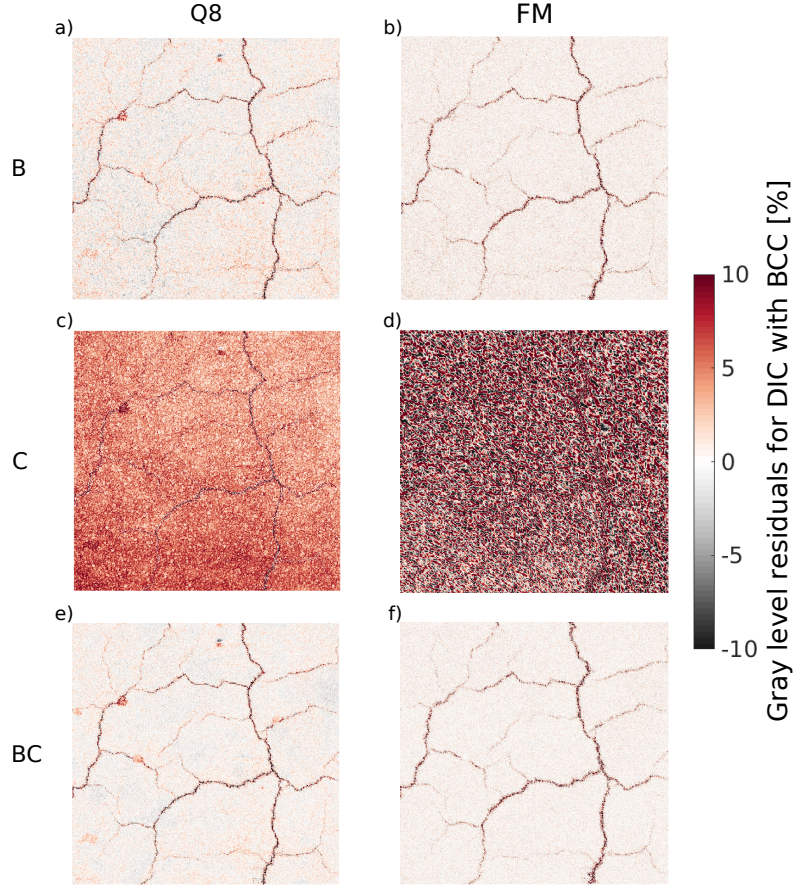


Figure 6: Normalized gray level residuals (in % of dynamic range) for the last image captured during curing and drying when three corrections: brightness (B), contrast (C), brightness and contrast (BC) were carried out with two discretizations (Q8 and FM)

Pores are regions with low contrast, *i.e.*, regions with uniform dark gray 280  
pixels due to the shadow formed by the depth of these artifacts (Figure 1), which 281  
may be considered as defects and corrected by the BCC procedures. Besides, 282  
the cracks create new gray levels during their opening, as mentioned herein, 283  
which makes them an additional source of gray level variation. However, the 284  
cracks caused by MgO hydration and their quantification are the main objective 285  
for the present case study. If the corrections affect the detection of cracks, it is 286  
important to check the effect of BCCs on their representation. One can notice 287

that the Q8 discretization shows high values of gray level residuals in porous regions (*i.e.*,  $\approx 5\%$ ), for B or BC corrections. Though, the residuals are low for the same regions in the FM results ( $\approx 0.5\%$ ), which means that the FM can correct such effect thanks to the high number of nodes, and the element size close to the pore one (Figure 1), *i.e.*, enough DOFs (80,000 for FM BC). Conversely, the FM correction spreads the gray level residuals in the cracked regions. It may compromise the evaluation of the crack positions. The effect of smeared residuals around cracks is reduced in the Q8 results because of the minimal number of DOFs (16 for Q8 BC) that ignores the effect of the pores, and also reduces the issue in crack detection.

The results obtained by different BCCs are further compared using histograms of gray level residuals (Figure 7). The histograms for C corrections using both discretizations are close to those with no BCC. The FM C case increased the range of gray level residuals by  $\approx 30\%$ , thereby showing a lower quality of the results. Such effect is due to the coupling of contrast correction and the kinematic, which should be avoided [32]. The other corrections (*i.e.*, B and BC) resulted in distributions centered about zero for both discretizations, which are significantly lower for the FM one. This shape is expected for the standard acquisition noise, which usually is white and Gaussian as a first approximation [32]. Further, there are many pixels close to zero gray level residuals that correspond to regions with no crack (*i.e.*, clusters of aggregates). Comparing B and BC results for both discretizations, B resulted in slightly wider distributions because it uses two times fewer DOFs.

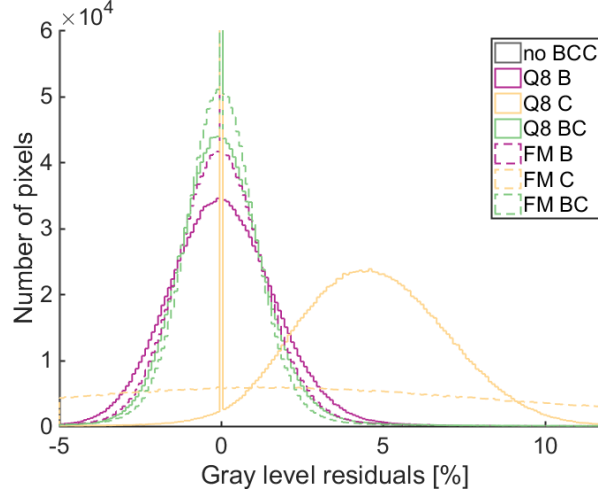
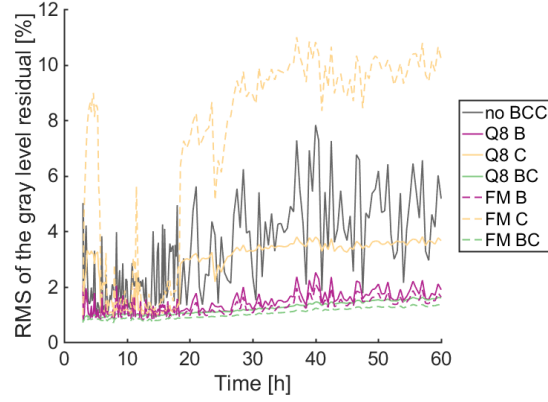


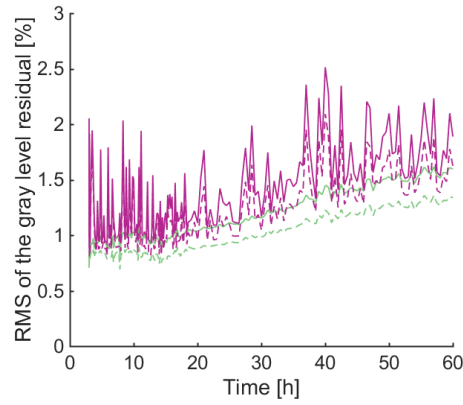
Figure 7: Histograms of gray level residuals (in % of dynamic range) for all BCC procedures tested herein using the last image of the experiment

The frame-wise RMS of the gray level residuals is reported for the image  
set #2 (*i.e.*, entire experiment) in Figure 8. The DIC result with no BCC  
is related to various sources of gray level changes such as lighting and vapor  
stream. The C correction performed poorly compared to B and BC. Further,  
the FM C analysis randomly increased the fluctuations in different frames. In  
the present case, such corrections should not be used. Conversely, the RMS  
residuals were significantly reduced with B and BC corrections, from an average  
RMS of 5% for DIC with no BCC to 1.5% for B and BC corrections. Last, the  
RMS levels start to increase after frame 100 for all corrections. This trend is  
related to the opening of numerous cracks, *i.e.*, they are one source of gray level  
residuals even when corrections with many DOFs (FM B and FM BC) are used.





(a)



(b)

Figure 8: RMS residuals (in % of dynamic range) for the six BCC analyses. (a) All analyses. (b) Details for the sets of parameters with smaller RMS residuals. The BCC using coarse or fine discretizations reduced the residual levels when compared to DIC with no BCC

In Figure 8(b), the three cases with higher RMS residuals (*i.e.*, no BCC and C corrections with both discretizations) are excluded to make easier the comparison between B and BC results. The BC correction for Q8 and FM reduced the residuals, and increased the difference between the results of the two discretizations for B, which indicates that BC is more sensitive to the mesh type than B. However, the mean difference of RMS residuals between B and BC

corrections remains small (*i.e.*,  $\approx 0.5\%$  of the dynamic range).

The maximum principal strain  $\epsilon_1$  fields for the last image of the experiment (frame 200) were obtained using all BCC procedures (Figure 9).

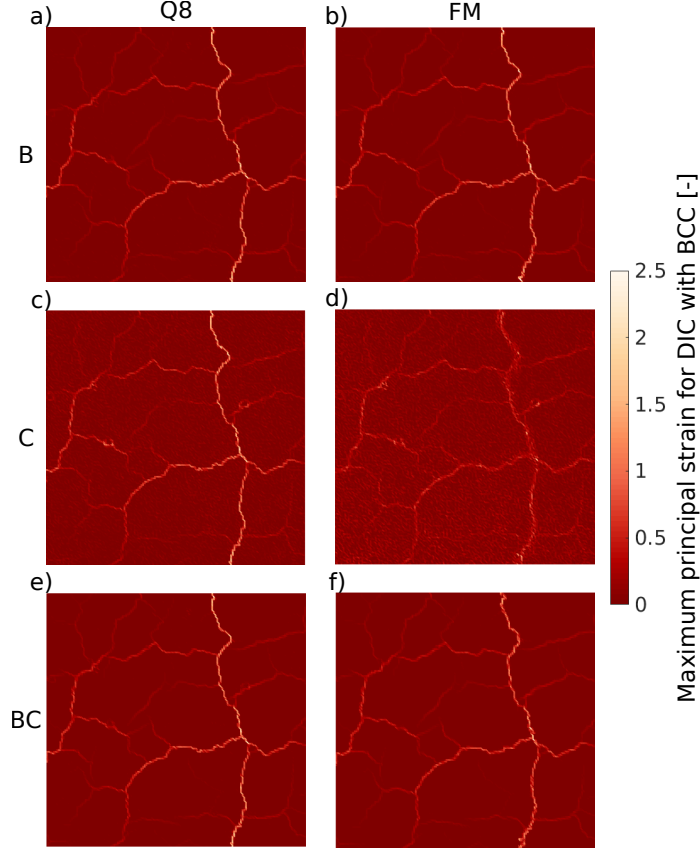


Figure 9: Maximum principal strain (dimensionless) field for the last image acquired during the experiment using the corrections: brightness (B), contrast (C), brightness and contrast (BC), carried out with two discretizations (Q8 and FM)

The levels of  $\epsilon_1$  are uniform, mainly for B and BC corrections and close to zero in cluster regions, which is different for the grainy fields obtained using DIC with no BCC (see Figure 5(b)). The low strain regions are expected because the MgO hydration is a heterogeneous expansion that occurs in the matrix of the castable [46]. The B and BC corrections allowed small cracks to be detected (*i.e.*,

elements with low  $\epsilon_1$  levels), which were more difficult to spot in DIC results with  
no BCC. Further, the effect of the pores mentioned in the gray level residuals is  
not observed in the strain fields for the cases using the FM discretization. The  
latter erases spurious gray level variations caused by the pores. However, they  
may lead to higher strain levels, which would be considered as cracks in some  
analyses, such as the crack density [48], and thereby reduce the accuracy of the  
damage evaluation.

The BCCs reduced not only the effect of the pores but also that one of  
the cracks, which are localized sources of gray level changes. This phenomenon  
causes the appearance of elements with very small  $\epsilon_1$  in the crack path as if the  
BCCs tried to close the cracks. It is mainly relevant for corrections using FM  
because this discretization has more DOFs that enable BCCs to act in localized  
segments of the surface of interest. FM C corrections resulted in a grainy field  
caused by their coupling with the underlying kinematics. The FM B and FM  
BC routes led to similar  $\epsilon_1$  fields, except for the apparent wider cracks in FM  
BC and their levels smaller than the FM B results. To make the comparison  
easier between the fields of a pair of BCCs, their differences  $\Delta\epsilon_1$  are reported  
in Figure 10.

As the case study discussed in this paper concerns the monitoring of open  
cracks, it means that the maximum principal strain  $\epsilon_1$  is always positive. This  
feature is useful to distinguish the effect of each BCC by the level in the  $\Delta\epsilon_1$   
fields of Figure 10. For example, in Q8 B - Q8BC  $\Delta\epsilon_1$  (Figure 10(a)) the blue  
artifacts are due to Q8 BC, because it represents negative values in the color  
map. These artifacts are pore effects that were better corrected by Q8 B than  
Q8 BC. In the strain difference FM B - FM BC, no pore effect is observed  
in Figure 10(b). However, they can be seen in red in Figures 10(c,d), and  
are attributed to Q8 B and Q8 BC, respectively. These results confirm the  
hypothesis that the FM procedures correct the pore effects, but the Q8 ones  
do not. Such feature of the FM procedures is due to the localized effect of  
the corrections provided by the higher number of DOFs (*i.e.*, 40,000 for B and  
80,000 for BC corrections).

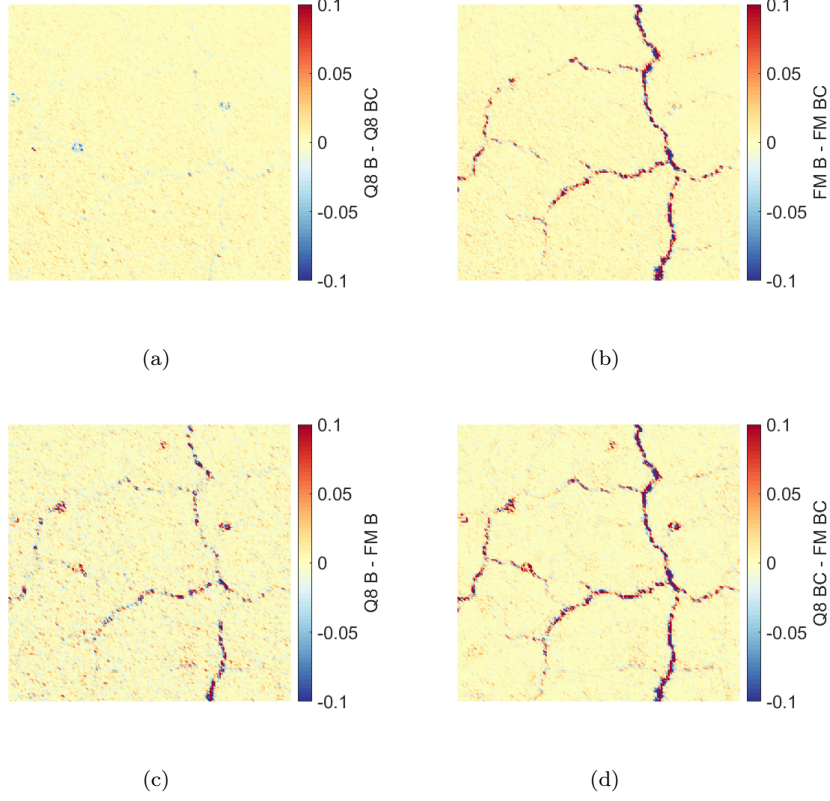


Figure 10: Difference of maximum principal strain fields  $\Delta\epsilon_1$  (dimensionless) between: (a) Q8 B and Q8 BC, (b) FM B and FM BC, (c) Q8 B and FM B, and (d) Q8 BC and FM BC to show how different corrections affect the cracks. The range of the color map was reduced to improve the contrast

The effect of the BCCs on the crack opening (or equivalently on the strain fields) is analyzed in the sequel. In Figure 10(b), a red crack path due to FM B is mostly surrounded by blue levels provided by FM BC corrections. Red crack paths (Figures 10(c,d)) are due to Q8 corrections, which do not have a localized effect, as observed for correcting the pore effects. The paths are surrounded by the same blue artifacts, which are due to FM B and FM BC corrections that spread the grey level residuals and, consequently, reduce the  $\epsilon_1$  levels in the main paths and increase it in some adjacent elements.

Histograms are also used to compare different distributions for the  $\epsilon_1$  fields

(Figure 11). The vertical axis is represented in logarithmic scale to make possible the visualization of the number of elements with high  $\epsilon_1$  levels. Similar to the histograms obtained for the gray level residuals, the C corrections, mainly the FM C, are not efficient since they are close to the strain distributions of DIC with no BCC. The other corrections led to distributions with a higher number of elements in low and high strains than in DIC with no BCC, *i.e.*, there is a clear separation of cluster zones ( $\epsilon_1 \approx 0$ ) and cracks (high  $\epsilon_1$ ). Moreover, the distributions are very similar for B and BC corrections using both discretizations. Large crack openings led to deviations, mainly for the FM BC, which showed fewer elements in high  $\epsilon_1$  because this procedure has a strong localized effect and corrects the increase in gray level residuals due to cracks.

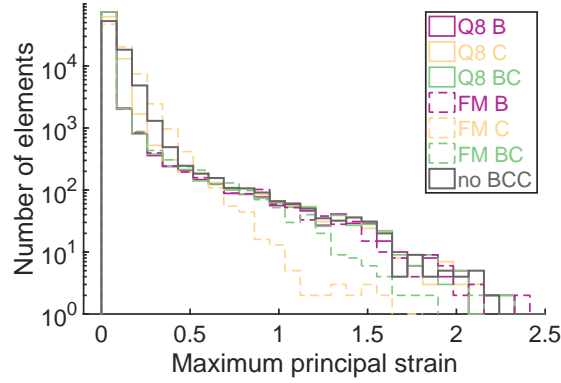
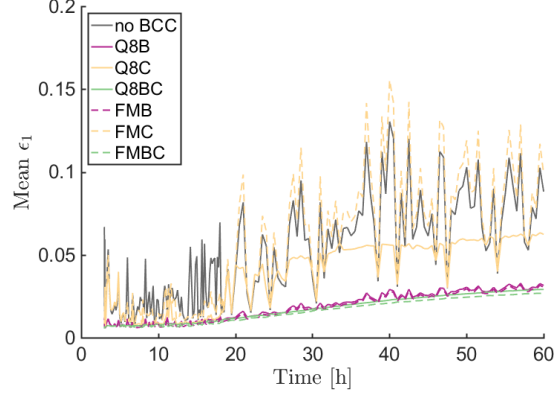


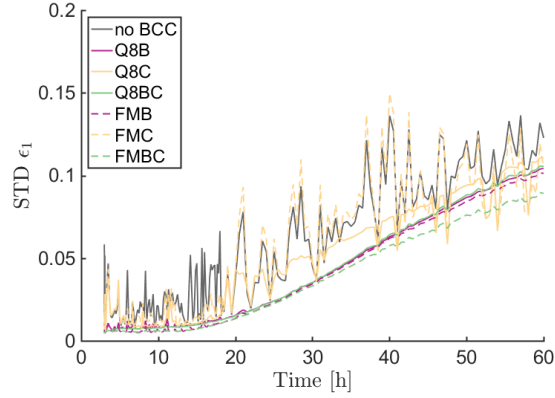
Figure 11: Histograms of maximum principal strain (dimensionless) for all BCC procedures using the last image of the experiment

The mean and standard deviation of maximum principal strains are plotted as a function of time (Figure 12). As expected from the previous analyses, the C corrections are very close to DIC with no BCC throughout the whole history. They are fluctuating in time a lot more than the other corrections, which are consistent for both reported quantities. The differences between the various corrections are more important on the mean levels of  $\epsilon_1$  than on its standard

deviation. This observation proves that when the corrections are not optimal, the mean  $\epsilon_1$  is over-estimated.



(a)



(b)

Figure 12: Evolution of mean (a) and standard deviation (b) of maximum principal strain (dimensionless) during 60 h of curing and drying

By considering all the previous results, it is concluded that only the contrast correction is not advisable as it led to results very close to those with no correction at all. The brightness and contrast correction is the best type (as it lowers the residuals the most) even though the brightness correction alone also gave good results. The small number of DOFs required with one Q8 element

makes it the best choice for the discretization.

#### 4. Conclusion

A case study where a refractory cube was kept in a climatic chamber during curing and drying was presented. Inside the chamber, the vapor stream and the temperature (50°C) acted all over the surface of interest, thereby inducing gray level changes. Besides, there were two localized sources of gray level variation, namely, open pores on the photographed surface and cracks, which were due to the hydration of MgO present in the castable formulation. Brightness and contrast corrections (BCCs) were performed in the registration, namely brightness (B), contrast (C), and brightness and contrast (BC). The BCCs made use of two discretizations for the same region of interest: one 8-noded quadrilateral element (Q8) and a fine mesh (FM with 5-px triangular elements) also used to measure displacement fields. The acquired images were divided into set #1 composed of 10 images at the beginning of the experiment (*i.e.*, before crack initiation), and set #2 covering the whole experiment. Set #1 was used to analyze the performance of the BCCs against the effects of vapor stream and the temperature, whereas the goal of BCCs with set #2 was to correct the pore effect without compromising the crack quantification.

The uncertainty quantifications (with set #1) showed that all BCCs were able to lower the gray level residuals due to experimental variations of lighting with no cracks. BC corrections led to the lowest displacement and strain uncertainties for both discretizations, which were one order of magnitude less than DIC results with no BCC. Conversely, B and C corrections were discretization-dependent. Such results highlight the gains that can be expected if such corrections are implemented.

BCCs significantly reduced the gray level residuals in the presence of cracks. The coupling between C corrections and cracks made them ineffective. B and BC corrections resulted in maximum principal strain and gray level residual fields with high values mostly concentrated in the cracked regions, and lower values

in the zones around them containing aggregate clusters. This result enabled  
the visualization of small cracks that were difficult to pinpoint via DIC with  
no BCC. The Q8 discretization should be selected to avoid interpreting pores  
as cracks because it fully decouples the very details of the kinematics from BC  
corrections. It is worth noting that finer meshes (*e.g.*, of the characteristic size  
that of pores) but not as fine as that used for capturing the complex kinematics  
induced by crack networks could also be investigated in the future to confirm  
this hypothesis.

The above discussions showed that BCCs were desirable in the case studied  
herein as they led to significant gains in terms of noise-floor levels and detection  
of very localized features (*i.e.*, cracks). Special care should be exercised in  
the choice of discretization since it may lead to undesired couplings with the  
underlying kinematics. BCCs provide additional DOFs that have to be selected  
with good understanding of the phenomena at stake in the studied experiment  
(*e.g.*, illumination conditions, image modality, kinematic basis). Once properly  
selected, they mitigate temporal fluctuations (Figure 12) that are nonphysical  
with no need for other regularization strategy.

## Authors' contributions

VS, RBC, FH designed the experiments. VS performed the experiments,  
analyzed the data, and drafted the manuscript. VS, JN, FH implemented the  
computer code and supporting algorithms. RBC and FH provided the materials  
and computing resources. All authors reviewed and approved this version of the  
manuscript.

## Acknowledgements

This study was financed in part by the Coordenação de Aperfeiçoamento de  
Pessoal de Nível Superior – Brasil (CAPES) – Finance Code 001. V. S. would  
also like to thank CAPES for the PDSE grant # 8881.188511/2018-01 used  
during the internship at LMT. This study was also partially supported by the



FAPESP-CNRS SPRINT project, grant #2018/15266-0, São Paulo Research  
Foundation (FAPESP). The authors would like to thank prof. Victor Carlos  
Pandolfelli for the discussions about the present work.

## References

- [1] Sutton MA, McNeill SR, Helm JD, Chao YJ. Advances in  
two-dimensional and three-dimensional computer vision; vol. 77 of  
Topics in Applied Physics. 2000.
- [2] Sutton MA, Orteu JJ, Schreier H. Image correlation for shape, motion  
and deformation measurements: Basic concepts, theory and applications.  
Springer Science & Business Media; 2009.
- [3] Bay B. Methods and applications of digital volume correlation. J Strain  
Analysis 2008;43:745–60.
- [4] Buljac A, Jailin C, Mendoza A, Taillandier-Thomas T, Bouterf A, Neggers  
J, et al. Digital Volume Correlation: review on progress and challenges.  
Exp Mech 2018;58(5):661–708.
- [5] Sutton MA. Computer vision-based, noncontacting deformation measure-  
ments in mechanics: A generational transformation. Applied Mechanics  
Reviews 2013;65(AMR-13-1009, 050802).
- [6] Lyons JS, Liu J, Sutton MA. High-temperature deformation measurements  
using digital-image correlation. Experimental Mechanics 1996;36(1):64–70.
- [7] Sutton MA, Wolters WJ, Peters WH, Ranson WF, McNeill SR. Deter-  
mination of displacements using an improved digital correlation method.  
Image and Vision Computing 1983;1(3):133 –9.
- [8] Maynadier A, Poncelet M, Lavernhe-Taillard K, Roux S. One-shot measure-  
ment of thermal *and* kinematic fields: Infra-red image correlation (IRIC).  
Experimental Mechanics 2011;52(3):241–55.

- [9] Charbal A, Roux S, Hild F, Vincent L. Spatiotemporal regularization for digital image correlation: Application to infrared camera frames. *International Journal for Numerical Methods in Engineering* 2018;114(12):1331–49.
- [10] Sutton MA, Li N, Joy D, Reynolds AP, Li X. Scanning Electron Microscopy for quantitative small and large deformation measurements part I: SEM imaging at magnifications from 200 to 10,000. *Experimental Mechanics* 2007;47(6):775–87.
- [11] Sutton MA, Li N, Garcia D, Cornille N, Orteu JJ, McNeill SR, et al. Scanning electron microscopy for quantitative small and large deformation measurements part II: Experimental validation for magnifications from 200 to 10,000. *Experimental Mechanics* 2007;47(6):789–804.
- [12] Bay BK, Smith TS, Fyhrie DP, Saad M. Digital volume correlation: three-dimensional strain mapping using X-ray tomography. *Experimental Mechanics* 1999;39:217–26.
- [13] Hild F, Bouterf A, Roux S. Damage measurements via DIC. *International Journal of Fracture* 2015;191(1-2):77–105.
- [14] Vargas R, Neggers J, Canto RB, Rodrigues JA, Hild F. Comparison of two full-field identification methods for the wedge splitting test on a refractory. *Journal of the European Ceramic Society* 2018;38(16):5569–79.
- [15] Vargas R, Neggers J, Canto RB, Rodrigues JA, Hild F. Analysis of a castable refractory using the wedge splitting test and cohesive zone model. *Journal of the European Ceramic Society* 2019;39(13):3903–14.
- [16] Chevalier L, Calloch S, Hild F, Marco Y. Digital image correlation used to analyze the multiaxial behavior of rubber-like materials. *European Journal of Mechanics-A/Solids* 2001;20:169–87.
- [17] Hild F, Raka B, Baudequin M, Roux S, Cantelaube F. Multi-scale displacement field measurements of compressed mineral wool samples by digital image correlation. *Appl Optics* 2002;IP 41(32):6815–28.

- [18] Novak MD, Zok FW. High-temperature materials testing with full-field strain measurement: Experimental design and practice. Review of Scientific Instruments 2011;82(11):115101.
- [19] Lucas BD, Kanade T. An iterative image registration technique with an application to stereo vision. In: 7th International Joint Conference on Artificial Intelligence. 1981, p. 674–9.
- [20] Chu T, Ranson W, Sutton M, Peters W. Applications of digital-image-correlation techniques to experimental mechanics. Experimental Mechanics 1985;3(25):232–44.
- [21] Tong W. An evaluation of digital image correlation criteria for strain mapping applications. Strain 2005;41(4):167–75.
- [22] Pan B. Recent progress in digital image correlation. Experimental Mechanics 2011;51:1223–1235.
- [23] Peng B, Zhang Q, Zhou W, Hao X, Ding L. Modified correlation criterion for digital image correlation considering the effect of lighting variations in deformation measurements. Optical Engineering 2012;51(1):1–5.
- [24] Kammers AD, Daly S. Digital image correlation under scanning electron microscopy: Methodology and validation. Experimental Mechanics 2013;53(9):1743–61.
- [25] Meyer P, Waas AM. Measurement of in situ-full-field strain maps on ceramic matrix composites at elevated temperature using digital image correlation. Experimental Mechanics 2015;55(5):795–802.
- [26] Grant BMB, Stone HJ, Withers PJ, Preuss M. High-temperature strain field measurement using digital image correlation. Journal of Strain Analysis for Engineering Design 2009;44(4):263–71.
- [27] Pan B, Wu D, Xia Y. High-temperature deformation field measurement by combining transient aerodynamic heating simulation system and

- reliability-guided digital image correlation. *Optics and Lasers in Engineering* 2010;48(9):841–8. 538  
539
- [28] Archer T, Beauchene P, Huchette C, Hild F. Global digital image correlation up to very high temperatures with grey level corrections. *Measurement Science and Technology* 2020;31(2):024003. 540  
541  
542
- [29] Lewis JP. Fast template matching. In: *Vision interface*; vol. 95. 1995, p. 15–9. 543  
544
- [30] Gao G, Yao W, Xia K, Li Z. Investigation of the rate dependence of fracture propagation in rocks using digital image correlation (DIC) method. *Engineering Fracture Mechanics* 2015;138:146–55. 545  
546  
547
- [31] Su YQ, Yao XF, Wang S, Ma YJ. Improvement on measurement accuracy of high-temperature DIC by grayscale-average technique. *Optics and Lasers in Engineering* 2015;75:10–6. 548  
549  
550
- [32] Hild F, Roux S. Digital image correlation. In: Rastogi P, Hack E, editors. *Optical Methods for Solid Mechanics. A Full-Field Approach*. Weinheim (Germany): Wiley-VCH; 2012, p. 183–228. 551  
552  
553
- [33] Charbal A, Vincent L, Hild F, Poncelet M, Dufour JE, Roux S, et al. Characterization of temperature and strain fields during cyclic laser shocks. *Quantitative InfraRed Thermography Journal* 2016;13(1):1–18. 554  
555  
556
- [34] Charbal A, Cinoglu I, Hild F, Roux S, Vermaak N. Stereocorrelation Formalism Considering Brightness and Contrast Effects: Application to Torsional Loadings. *Experimental Mechanics* 2020;doi:10.1007/s11340-019-00576-2. 557  
558  
559  
560
- [35] Wang Y, Charbal A, Dufour J, Hild F, Roux S, Vincent L. Hybrid multiview correlation for measuring and monitoring thermomechanical fatigue test. *Experimental Mechanics* 2020;60(1):13–33. 561  
562  
563

- [36] Mendoza A, Schneider J, Parra E, Obert E, Roux S. Differentiating 3D textile composites: A novel field of application for Digital Volume Correlation. Composite Structures 2019;208:735–43.
- [37] Mendoza A, Schneider J, Parra E, Roux S. The correlation framework: bridging the gap between modeling and analysis for 3D woven composites. Composite Structures 2019;78:111468.
- [38] Ciddor PE. Refractive index of air: new equations for the visible and near infrared. Applied optics 1996;35(9):1566–73.
- [39] Robert L, Nazaret F, Cutard T, Orteu JJ. Use of 3D digital image correlation to characterize the mechanical behavior of a fiber reinforced refractory castable. Experimental Mechanics 2007;47(6):761–73.
- [40] Belrhiti Y, Pop O, Germaneau A, Doumalin P, Dupré JC, Harmuth H, et al. Investigation of the impact of micro-cracks on fracture behavior of magnesia products using wedge splitting test and digital image correlation. Journal of the European Ceramic Society 2015;35(2):823–9.
- [41] Vargas R, Neggers J, Canto RB, Rodrigues JA, Hild F. Analysis of wedge splitting test on refractory castable via integrated DIC. Journal of the European Ceramic Society 2016;36(16):4309–17.
- [42] Sutton MA, Zhao W, McNeill SR, Helm JD, Piascik RS, Riddell WT. Advances in fatigue crack closure measurement and analysis: Second Volume; chap. Local crack closure measurements: Development of a measurement system using computer vision and a far-field microscope. West Conshohocken: ASTM STP 1343; 1999, p. 145–56.
- [43] Rupil J, Roux S, Hild F, Vincent L. Fatigue microcrack detection with digital image correlation. The Journal of Strain Analysis for Engineering Design 2011;46(6):492–509.
- [44] Benboudjema F, Mauroux T, Turcry P, Ait-Mokthar A, Deves O. Experimental analysis of drying shrinkage cracking in coating mortars by digital

- image correlation. In: Mechanics and Physics of Creep, Shrinkage, and Durability of Concrete: A Tribute to Zdeněk P. Bažant: Proceedings of the Nineth International Conference on Creep, Shrinkage, and Durability Mechanics (CONCREEP-9), September 22-25, 2013 Cambridge, Massachusetts. ASCE Publications; 2013, p. 235.
- [45] Saracura RGM, Canto RB, Pandolfelli VC, Schmitt N, Hild F. Surface crack network detection on MgO-based refractory castable by digital image correlation. *China's Refractories* 2015;24(1):32–7.
- [46] Salomão R, Pandolfelli VC. The role of hydraulic binders on magnesia containing refractory castables: calcium aluminate cement and hydratable alumina. *Ceramics International* 2009;35(8):3117–24.
- [47] ASTM C1424-15. Standard test method for monotonic compressive strength of advanced ceramics at ambient temperature. Tech. Rep.; ASTM International; 2015.
- [48] Sciuti VF, Hild F, Pandolfelli VC, Santos T, Smaniotto B, Canto RB. Digital Image Correlation applied to *in situ* evaluation of surface cracks upon curing of MgO containing refractory castables. *Journal of the European Ceramic Society* 2020;doi:10.1016/j.jeurceramsoc.2020.04.055.
- [49] Leplay P, Lafforgue O, Hild F. Analysis of asymmetrical creep of a ceramic at 1350 °C by Digital Image Correlation. *Journal of the American Ceramic Society* 2015;98(7):2240–7.
- [50] Bayer BE. Color imaging array. 1976. US Patent 3,971,065.
- [51] Roux S, Hild F, Berthaud Y. Correlation image velocimetry: A spectral approach. *Applied Optics* 2002;41(1):108–15.
- [52] Wagne B, Roux S, Hild F. Spectral approach to displacement evaluation from image analysis. *European Physical Journal Applied Physics* 2002;17:247–52.

- [53] Broggiato GB. Adaptive image correlation technique for full-field strain measurement. In: Pappalettere C, editor. Proceedings of ICEM12-12th International Conference on Experimental Mechanics. McGraw Hill, Lilan (Italy); 2004, p. 420–1.
- [54] Sun Y, Pang J, Wong C, Su F. Finite-element formulation for a digital image correlation method. *Applied Optics* 2005;44(34):7357–63.
- [55] Besnard G, Hild F, Roux S. “Finite-Element” displacement fields analysis from digital images: Application to Portevin-Le Chatelier bands. *Experimental Mechanics* 2006;46(6):789–803.
- [56] Leclerc H, Neggers J, Mathieu F, Roux S, Hild F. Correli 3.0. 2015. IDDN.FR.001.520008.000.S.P.2015.000.31500.
- [57] Hild F, Roux S. Comparison of local and global approaches to digital image correlation. *Experimental Mechanics* 2012;52(9):1503–19.